Supporting Information For: Elucidating Piezoelectricity and Strain in Monolayer MoS_2 at the Nanoscale Using Kelvin Probe Force Microscopy

Alex C. De Palma[1], Xinyue Peng[2], Saba Arash[2], Frank Y. Gao[2], Edoardo Baldini[2], Xiaoqin Li[2], Edward T. Yu*[1,3]

[1] Materials Science and Engineering Program, Texas Materials Institute, University of Texas at Austin, Austin, Texas 78712, USA
[2]Department of Physics and Center for Complex Quantum Systems, The University of Texas at Austin, Austin, TX, 78712 USA

[3]Microelectronics Research Center, Department of Electrical and Computer Engineering, University of Texas at Austin, Austin, Texas 78758, USA

* Corresponding Author: Edward T. Yu - Email: ety@ece.utexas.edu

S1 Substrate Fabrication

The top electrode and nanomesa array are patterned using nanosphere lithography processes,[1–4] as illustrated in Figure S1. The starting substrate consists of an n++ Si substrate with 150 nm of thermally grown SiO_2. Drop casting is used to form a hexagonal close packed array of 3um polystyrene microspheres on the surface of water in a trough, which is then drained and evaporated to deposit the microspheres on the surface. Reactive ion etching using an O_2 plasma is employed to shrink the diameter of the spheres from 3um to ~2um. The top electrode is then deposited using E-beam evaporation, and consists of a bottom 5 nm Ti seed layer to facilitate adhesion followed by a 45 nm Au layer. The microspheres are then removed via sonication in toluene for 1 minute. The remaining structure is an Au layer containing a hexagonal array of circular holes with 2um diameter and 3um spacing. The nanomesas are then fabricated by first depositing 1.5um microspheres onto the sample surface in a hexagonal close-packed array. The substrate and the microspheres are simultaneously etched by a plasma containing a combination of O_2 and CHF_3.

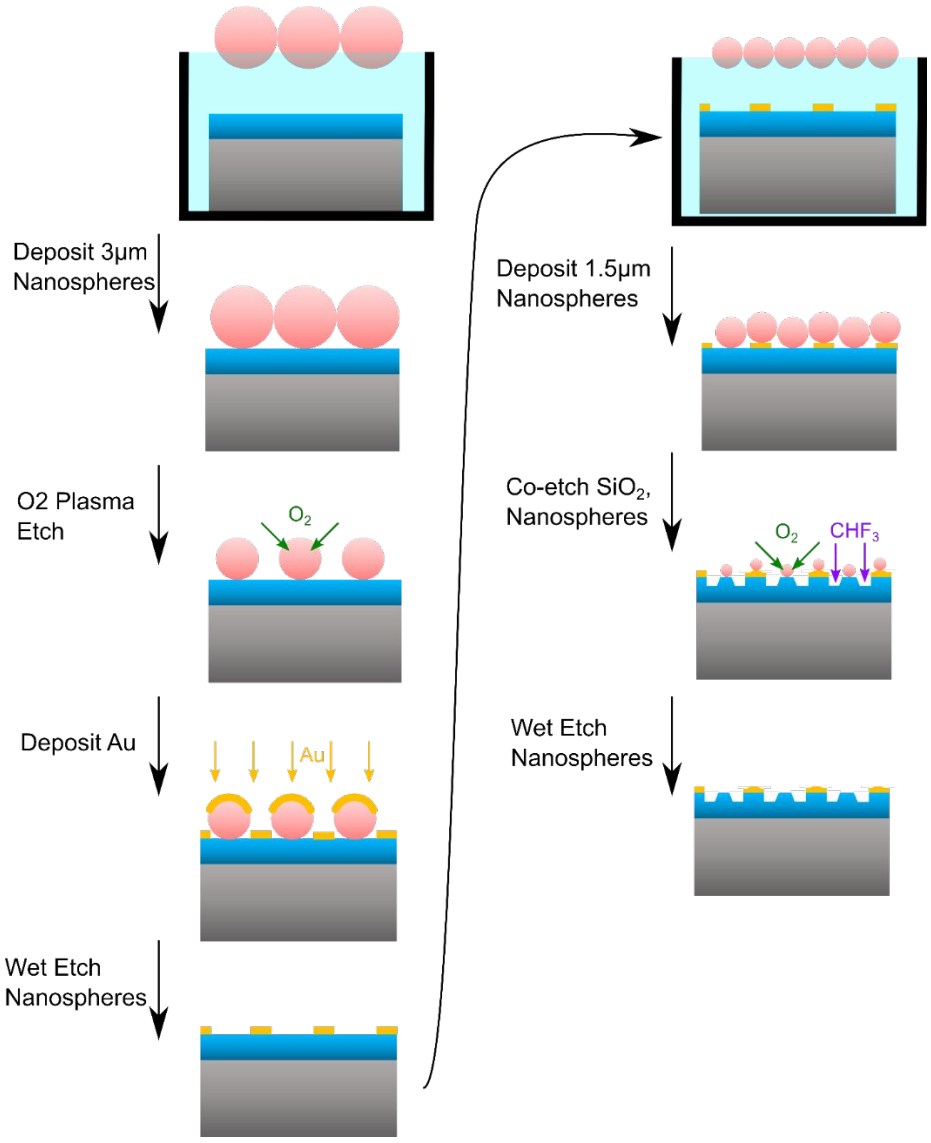

Figure S1 Process flow for substrate patterning using nanosphere lithography.

S2 MoS_2 Exfoliation and Transfer

MoS_2 is exfoliated from a bulk 2H crystal (2D Semiconductors) and transferred to the sample substrate using a PDMS dry transfer method.[5] The PDMS stamp is mounted face down on a glass slide fixed in place beneath an optical microscope. Below, on the microscope stage, the substrate is mounted faceup on top of a strip heater. The flake containing a monolayer region is then identified through the optical image of the

microscope and aligned to a suitable area of the substrate also identified using the microscope. The microscope stage is then gradually raised until the substrate comes into contact with the PDMS. A strip heater is then supplied with 2.1W of power, warming the substrate to ~70C. The PDMS and substrate are left in contact for 30 minutes before the strip heater is powered off. Contact is maintained for an additional 15 minutes to allow the sample to cool. The microscope stage is then gradually lowered until the PDMS and substrate are no longer in contact, leaving the MoS_2 flake transferred onto the substrate.

Raman spectroscopy and photoluminescence (PL) were used to identify monolayer regions of MoS_2. Optical characterization was performed using a 100x objective and an excitation laser wavelength of 532 nm at a laser power of 2 μW. Raman measurements were performed using an 1800 grooves/mm grating, and PL measurements were performed using a 300 grooves/mm grating. Characterization of the monolayer region is shown in Figure S2. The monolayer region is identified by the characteristic 20cm^{-1} separation of the Raman peaks[6,7] and the PL peak at 656 nm corresponding to the A exciton energy.[8]

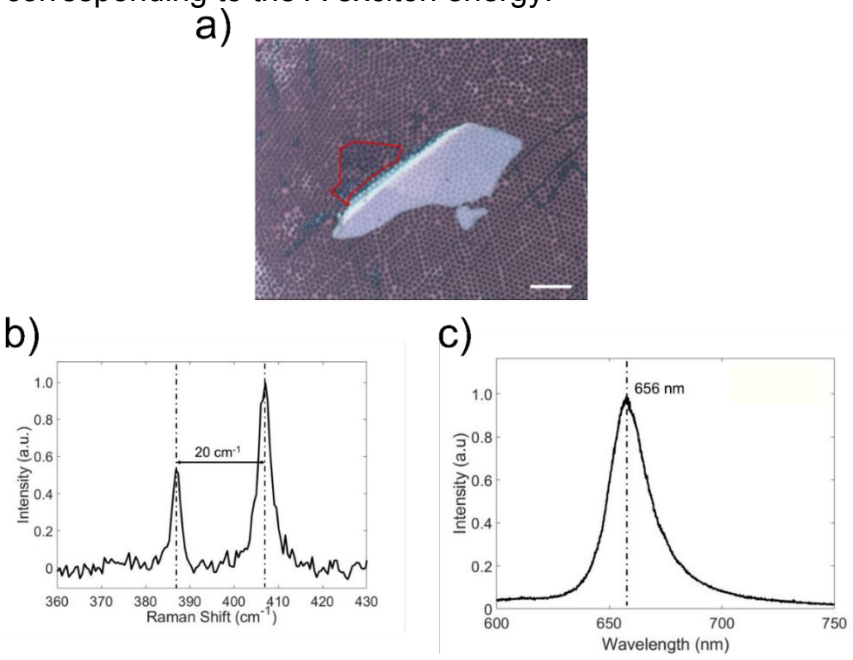

Figure S2 Characterization of the exfoliated MoS_2 flake after transfer to the patterned substrate. (a) Optical image of the flake, with monolayer region highlighted by the red border. (b) Raman and (c) PL characterization of the region within the red border, indicating monolayer MoS_2.

S3 Sample Topography

The fabricated sample structures consist of nanomesas embedded in circular holes with MoS_2 transferred on top. The nanomesa profile is relatively flat on top, with tapered edges, as shown in Figure S3a. Figure S3b shows the AFM topography of the nanomesa covered by monolayer MoS_2. The profiles of the nanomesas with and without MoS2 are comparable, suggesting that the MoS_2 is in approximately conformal contact with the nanomesa, with tenting around the tapered edges, as shown in the linecuts in Figure S3c.

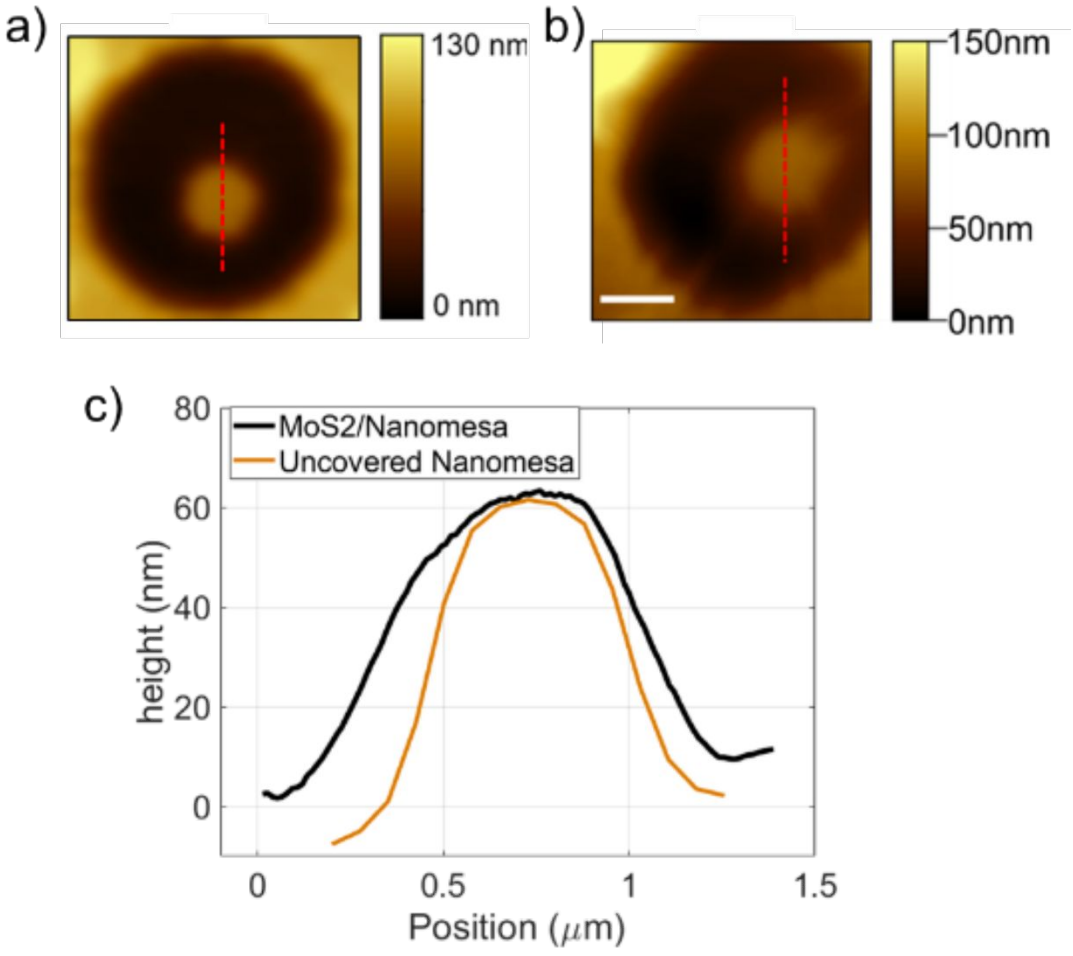

Figure S3 (a) AFM topography of an uncovered nanomesa centered in a circular hole region. (b) AFM topography of the nanomesa covered with monolayer MoS_2 presented in the main text. (c) Linecuts corresponding to the red dashed lines of the AFM data presented in (a) and (b).

S4 KPFM Methods

KPFM measurements are performed using an AIST Omegascope scanning probe system using a 2-pass method with lift height = 20 nm on the second pass for KPFM measurements, and an applied AC voltage with amplitude 2V and 1kHz frequency. The scan rate was 0.2 Hz on the first pass and 0.1 Hz on the second pass of KPFM measurements. Conductive Au-coated tips are used (OPUS 160AC GG) with cantilever spring constant 26 N/m and resonance frequency ~300kHz. Measurements were performed at room temperature in a dry N_2 environment (<5% RH) to minimize effects of humidity on gated KPFM measurements.

S5 Dependence of KPFM Measurements on Gate Voltage

The application of gate voltage, V_g, modifies the tip voltage, V_t, measured with KPFM. When no monolayer is present, as in Figure S4, variations in V_g correspond 1:1 to variations in V_t, indicating that surface contamination and humidity are hardly screening the applied field. There is also no observable contrast in V_t between the region with the nanomesa and the remainder of the flat SiO_2 region, indicating minimal effect of our etching procedure on introducing changed defects that might interfere with KPFM measurements.

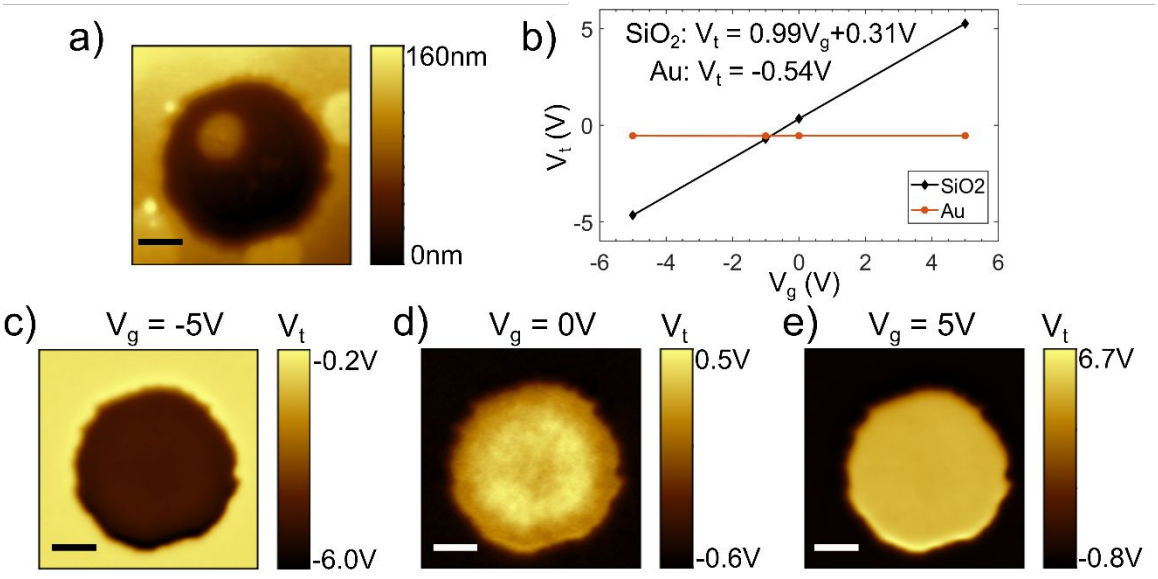

Figure S4 Dependence of V_t on V_g in a region without MoS_2. (a) The topography of the region measured with AFM. (b) Dependence of V_t on V_g for the gated SiO_2 region (within the circular hole) and the grounded Au region outside of the hole. The equation corresponds to the linear best fit for the dependence of V_t on V_g in the gated SiO_2 region. (c)(d)(e) KPFM images of V_t corresponding to the region in (a), for V_t=-5V, 0V, and 5V, respectively. The scale bars represent 500 nm.

Introducing the MoS2 monolayer affects the Vt vs. Vg dependence according to the quantum capacitance, C_q. To calculate the dependence of C_q on the Fermi level, we consider the total electron concentration in the conduction band of a two-dimensional n-type semiconductor, given by:

$$n = (g_{2D})(k_bT)\ln\left(1 + \exp\left[\frac{(E_F - E_C)}{k_bT}\right]\right), \quad (1)$$

where g_{2D} is the DOS of the conduction band of monolayer MoS_2 normalized to its thickness, k_b is the Boltzmann constant, T is the temperature (~300K), E_F is the Fermi level, and E_C is the conduction band edge energy. C_q is then:[9]

$$C_q = q^2\frac{\partial n}{\partial E_F} = q^2 g_{2D}\frac{\exp\left[(E_F - E_C)/k_BT\right]}{1 + \exp\left[(E_F - E_C)/k_BT\right]}, \quad (2)$$

where q is the elementary charge magnitude. Equation 2 was used to generate Figure 1c in the main text. As stated in the main text, this capacitance acts in series with the gate oxide capacitance, C_{ox}, such that the change of V_t due to V_g is given by

$$\frac{dV_t}{dV_g} = \frac{1}{\frac{C_q}{C_{ox}} + 1}. \quad (3)$$

Equations 2 and 3 are together used to calculate the dependence of V_t on V_g in Figure 1d in the main text.

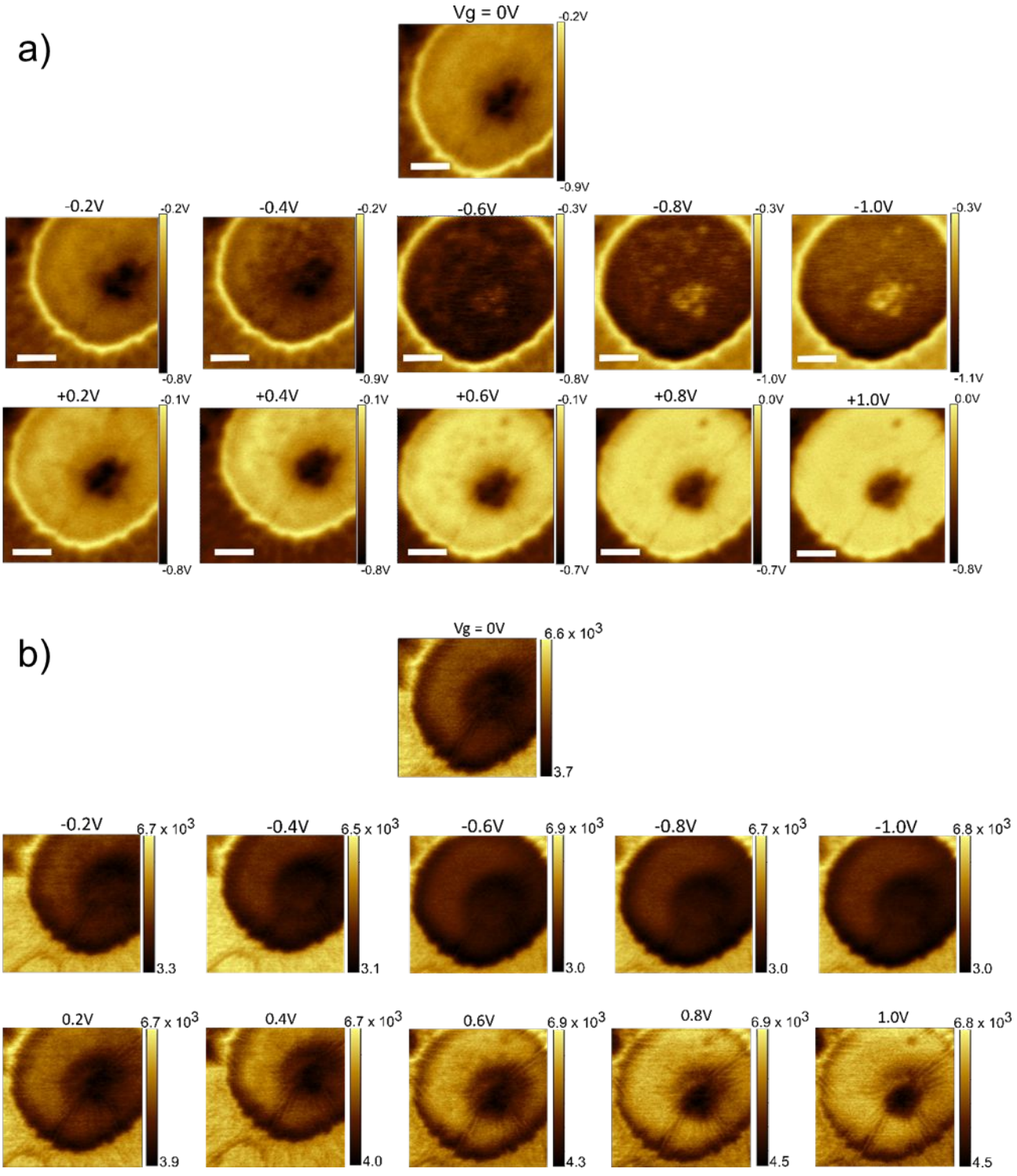

Figure S5 a) Vt and b) A2w KPFM images acquired at various Vg. Data was used to acquire data in Fig 2d of the main text.

S6 Converting KPFM Measurements to the Hydrostatic Strain Distribution

We can quantify the amount of strain in the vicinity of the nanomesa using the strain deformation potentials for the conduction band. We approximate the E_C deformation potential from the absolute uniaxial deformation potential at the K-point determined from DFT calculations.[10] These deformation potentials give the shift in the absolute energy of the conduction band using the vacuum energy as a reference, i.e. these deformation potentials directly correspond to changes in $\Delta(E_C - E_{vac})$, which is directly related to ΔV_t^{sat} in our KPFM measurement at V_g=5V. Therefore, the KPFM image can be converted to a mapping of the strain in the following way:

$$\Delta V_t^{sat} \approx a_k^{CBM} * (\Delta \varepsilon_{hyd}), \quad (4)$$

where a_k^{CBM} is the deformation potential of hydrostatic strain at the K-point in the Brillouin zone, which we approximate as 120meV/%,[10] and $\Delta \varepsilon_{hyd}$ is the spatial variation of the in-plane hydrostatic strain, which is related to the strain tensor as $\varepsilon_{hyd} = (\varepsilon_{11} + \varepsilon_{22})/2$. In this method, we are approximating that the shear and deviatoric strain deformation potentials are zero, which is a reasonable approximation at small strains.[11,12]

S7 Calculating strain in MoS_2 from AFM topography

We employ a method to calculate strain from the AFM topography that is similar to the method demonstrated by Darlington et. al. for TMD nanobubbles.[13] The method is mainly derived according to the theory of mechanics of thin plates, which can be found in introductory references on the subject[14] and will be briefly summarized here. Strain can be calculated from AFM topography using the Föppl-von Kármán equations describing the mechanics of thin plates subject to large out-of-plane deflections. Monolayer MoS_2

has a thickness much smaller than the lateral dimensions the flake and possesses negligible bending stiffness and it can be mechanically modeled as a thin plate. As a result, the stress components σ_{xz}, σ_{yz}, σ_{zz} are small compared to the other components of the stress tensor. The components of the in-plane strain tensor for plates are related to the stress by:

$$\varepsilon_{xx} = (\sigma_{xx} - \nu\sigma_{yy})/E, \quad (5)$$

$$\varepsilon_{yy} = (\sigma_{yy} - \nu\sigma_{xx})/E, \quad (6)$$

$$\varepsilon_{xy} = (1+\nu)\sigma_{xy}/E, \quad (7)$$

Where υ and E are the Poisson ratio and Young's modulus of MoS_2, respectively. The two-dimensional strain tensor for large transverse displacement of plates is given by:

$$\varepsilon_{\alpha\beta} = \frac{1}{2}\left(\frac{\partial u_\alpha}{\partial x_\beta} + \frac{\partial u_\beta}{\partial x_\alpha}\right) + \frac{1}{2}\frac{\partial h}{\partial x_\alpha}\frac{\partial h}{\partial x_\beta}, \quad (8)$$

where *u* is the in-plane displacement and *h* is the transverse displacement. The equations for equilibrium of thin plates are derived by minimizing the free energy, which has a bending and stretching component. The equations of equilibrium, termed the Föppl-von Kármán equations, are:

$$D\nabla^4 h - t\frac{\partial}{\partial x_\beta}\left(\sigma_{\alpha\beta}\frac{\partial h}{\partial x_\alpha}\right) = P, \quad (9)$$

$$\frac{\partial \sigma_{\alpha\beta}}{\partial x_\beta} = 0, \quad (10)$$

where D is the bending stiffness, t is the thickness of the monolayer, and P is the external normal force per unit area. Solving these equations can be simplified by introducing the Airy stress function, χ, defined by:

$$\sigma_{xx} = \frac{\partial^2\chi}{\partial y^2}, \sigma_{yy} = \frac{\partial^2\chi}{\partial x^2}, \sigma_{xy} = -\frac{\partial^2\chi}{\partial x \partial y}. \quad (11)$$

With the Airy stress function defined in this way, the Föppl-von Kármán equations can be reduced from 3 to 2, since Equation 10 is automatically satisfied. A new equation can be derived by substituting Equations 8 and 11 into Equations 5-7 to derive an additional equation in terms of the stress function:

$$\nabla^4\chi + E\left\{\frac{\partial^2 h \partial^2 h}{\partial x^2 \partial y^2} - \left(\frac{\partial^2 h}{\partial x \partial y}\right)^2\right\} = 0. \quad (12)$$

Equations 9 and 12 then form a complete system of equations for deflection of large plates. In principle, Equations 9 and 12 could be used to determine the deflection of plates for a given P; however, since we already know the deflection of the plate from the AFM topography, the stresses and strains can be readily obtained by solving for χ using Equation 12 alone. In order to solve this biharmonic equation for the stress function, we treat the problem as two weakly coupled Poisson equations: [13,15]

$$\nabla^2\psi = -E\left\{\frac{\partial^2 h \partial^2 h}{\partial x^2 \partial y^2} - \left(\frac{\partial^2 h}{\partial x \partial y}\right)^2\right\}, \quad (13)$$

$$\nabla^2\chi = \psi. \quad (14)$$

The procedure for solving for the strain is then to first solve Equation 13 using the gaussian curvature from the AFM topography, then solving Equation 14 using the result from solving Equation 13. It can be seen from the definition of the stress function that ψ is proportional to the trace of the in-plane stress tensor and therefore the hydrostatic strain. Solving for ψ gives a relation for the hydrostatic component of stress and strain derived from the height profile of the monolayer. Solving Equation 14 yields the remainder of the strain tensor, which is used to calculate the shear strain derived from the height profile of the monolayer. Figure S6 shows the shear strain solution derived from AFM data, defined as $\varepsilon_{\mathrm{shr}} = \sqrt{(\varepsilon\mathrm{xx} - \varepsilon\mathrm{yy})^2 + 4\varepsilon_{\mathrm{xy}}^2}$. The KPFM derived strain distribution does not resemble the shear strain distribution derived from AFM, further indicating that the KPFM observed contrast is due to primarily hydrostatic strain.

We assume the flat MoS_2 area atop the Au to be relatively unstrained. Since the MoS_2 beyond this boundary is relatively flat, the boundary condition ψ=0 is employed along the circular edge of the gated area. This boundary condition is equivalent to saying the change in area of the monolayer goes to zero on the flat area atop the Au electrode.

For the additional degrees of freedom, the boundary condition χ=0 is applied around a circular perimeter which encloses the entire area with a large radius. The choice of constant for χ on the boundary does not affect the stress/strain result, as the stress and strain are derived from the second derivatives of χ.

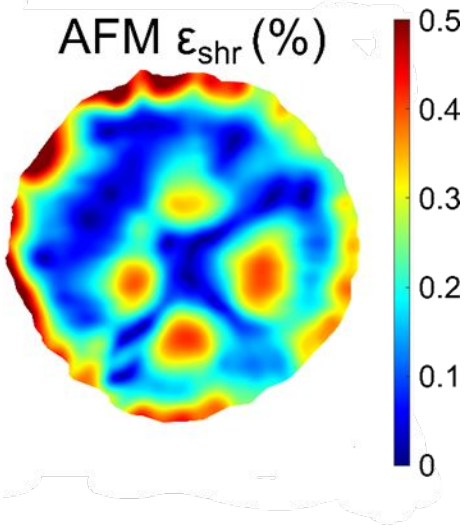

Figure S6. The in-plane shear component of the strain result derived from the topography.

S8 Curvature Extraction from AFM topography:

To extract the curvature data from AFM topography, local 3rd order polynomial surfaces were fit in a 7x7 pixel window around each point in the first pass of the AFM scan corresponding to the KPFM measurement at V_g=5V. Second derivatives at the central point of each surface were taken to be the second derivatives of the topography data at that point. The pixel spacing is ~20 nm, and each window contains a maximum of 1 inflection point in a 140 nm x 140 nm. The true topography could contain additional inflection points on smaller length scales, and the window size limits the lateral resolution of the curvature extraction; however, too small of a window size creates an unsmooth fitting due to noise in the AFM data. This is most prominently seen in the y derivatives, Figure S7d, which run perpendicular to the scan direction, as the drift between line scans is greater than the drift within a line scan along the x-axis. Median line filtering of the AFM

data is used to reduce this noise. The 7x7 pixel window size was selected to balance lateral resolution and data smoothness.

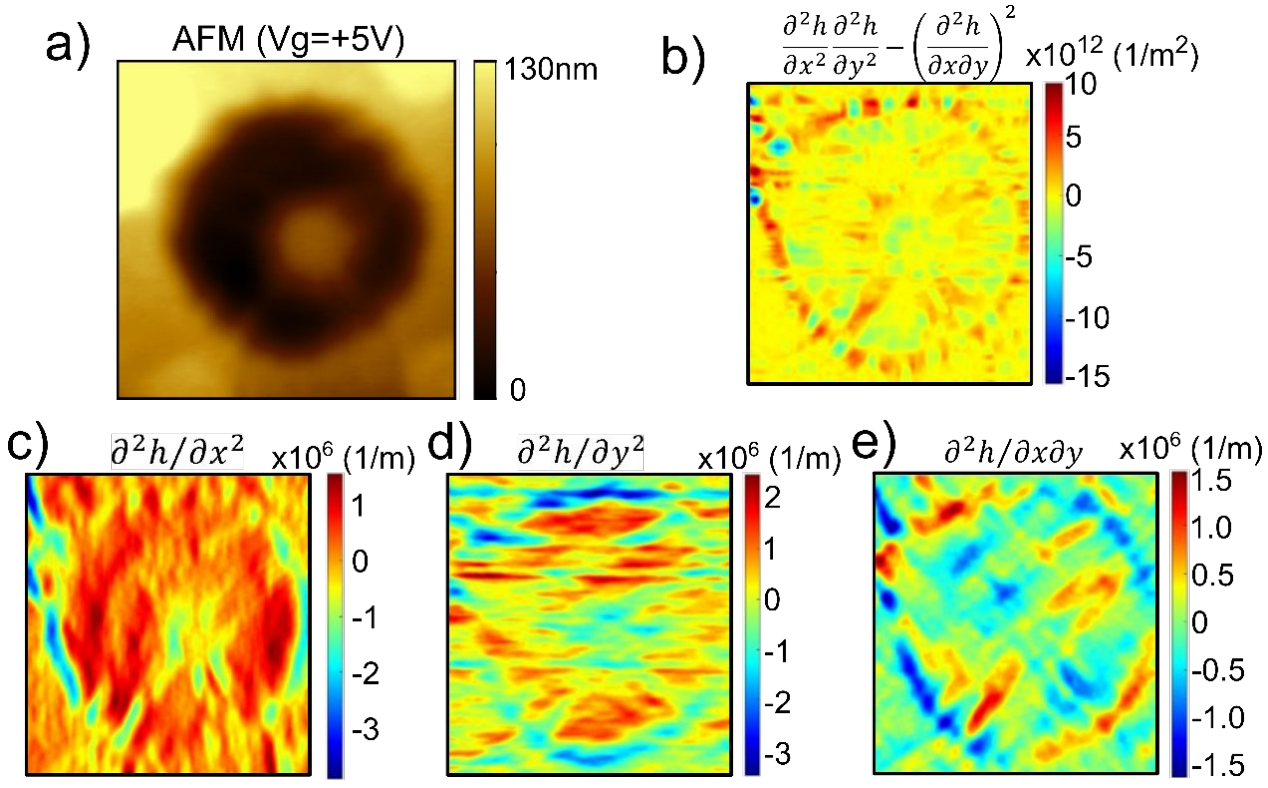

Figure S7 a) AFM topography used to derive curvature for strain calculations. b) The source term for Equation 3.21. (c), (d), (e) The individual components of the curvature of topography shown in (a).

S9 Determining the 2D strain tensor from the spatial variation of the hydrostatic strain

As stated in the main text, the Airy stress function is related to the hydrostatic strain distribution according to:

$$\nabla^2 \chi = \sigma_{xx} + \sigma_{yy} = \frac{2E}{1-\upsilon} * \varepsilon_{hyd}. \quad (15)$$

Solving Equation 15 for the Airy stress function provides the solution for the full strain tensor according via Equations 5-7 and 11. This step is equivalent to the second

step of the procedure for calculating the strain from the AFM topography using the Föppl-von Kármán equations, i.e. Equation 14, the difference being that for piezoelectric calculations we use ψ derived from the hydrostatic strain inferred from the KPFM measurement rather than from the solution to Equation 13. We set the boundary condition χ=0 around the circular perimeter of the gated area.

S10 CALCULATIONS OF PIEZOELECTRICITY:

The polarization field generated by piezoelectricity is then given by $P_i = e_{i\alpha}\varepsilon_\alpha$ where *e* is the piezoelectric tensor and ε is the strain in Voigt notation. The symmetry of the piezoelectric effect is determined by the symmetry of the lattice, and defined by the piezoelectric tensor, e, which for 2H crystals has the following form:

$$e = \begin{bmatrix} e_{11} & -e_{11} & 0 & 0 & 0 & 0 \\ 0 & 0 & 0 & 0 & 0 & -e_{11} \\ 0 & 0 & 0 & 0 & 0 & 0 \end{bmatrix}. \qquad (16)$$

The piezoelectricity tensor only has 1 unique coefficient, e_{11}, which is ~3.7x10^{-10} C/m for MoS_2.[16] The tensor defined in this way assumes an armchair direction along the x-axis and a zigzag direction along the orthogonal y-axis. In general, the lattice orientation is randomly aligned in relation to the AFM/KPFM coordinate system. Knowledge of the lattice orientation is required to properly calculate the effects of piezoelectricity.

We determine the orientation of the monolayer relative to our scan orientation using second harmonic generation (SHG). The two high-symmetry directions in MoS_2 are referred to as the armchair and zigzag directions, illustrated in Figure S8a. The response is largest along the armchair directions of the crystal lattice,[17] therefore, SHG

measurements allow us to determine the relative orientation between the armchair direction and the axis of previous KPFM measurements and strain calculations.

SHG measurements were performed using a Yb:YAG laser (Light Conversion, Carbide 40 W) with the repetition rate of 100 kHz and the pulse width of 150 fs. The 1030 nm laser beam was focused onto the sample using a ×50 microscope objective to a spot size of about 1 μm in diameter. A polarizing beamsplitter cube was placed before a longpass dichroic mirror to ensure the polarization uniformity of the excitation laser. In order to collect the polarimetry, a rotatable half wave plate was used to control the polarization of the excitation laser, while an analyzer was set in vertical and horizontal configurations in front of the detector to select the corresponding parallel and perpendicular SHG polar patterns. The SHG signal was passed through a 515 nm bandpass filter to filter the residual fundamental frequency, and then collected by a photomultiplier (Hamamatsu, H9305-01). The fast axis of the HWP is verified by aligning it with the fundamental beam using another properly aligned polarizer.

Monolayer MoS2 belongs to the D3h symmetry group, leaving the independent non-vanishing element of the nonlinear susceptibility to be $\chi_{yyy} = -\chi_{yxx} = -\chi_{xxy} = \chi_{xyx}$. Therefore, the dependence of SHG intensity on the rotation angle of the lattice, θ, follows

$$I_{\parallel} = I_0 cos(3\theta - 3c)^2 \quad (16)$$

$$I_{\perp} = I_0 sin(3\theta - 3c)^2 \quad (17)$$

where $I_{\parallel}$ and $I_{\perp}$ are the SHG intensity in the parallel and perpendicular polarization, respectively, and c is the relative offset of the armchair direction from the horizontal axis. The SHG data is shown in Figure S8. The SHG response is larger along one of the armchair directions, which could be the result of uniaxial strain.[18] Fitting the parallel and perpendicular polarization data in Figure S8(b,c) to Equations 16 and 17 respectively, we determine that the 3 armchair directions of the sample are at angles of 15, 135, and 255 degrees from the horizontal axis of KPFM and AFM measurements.

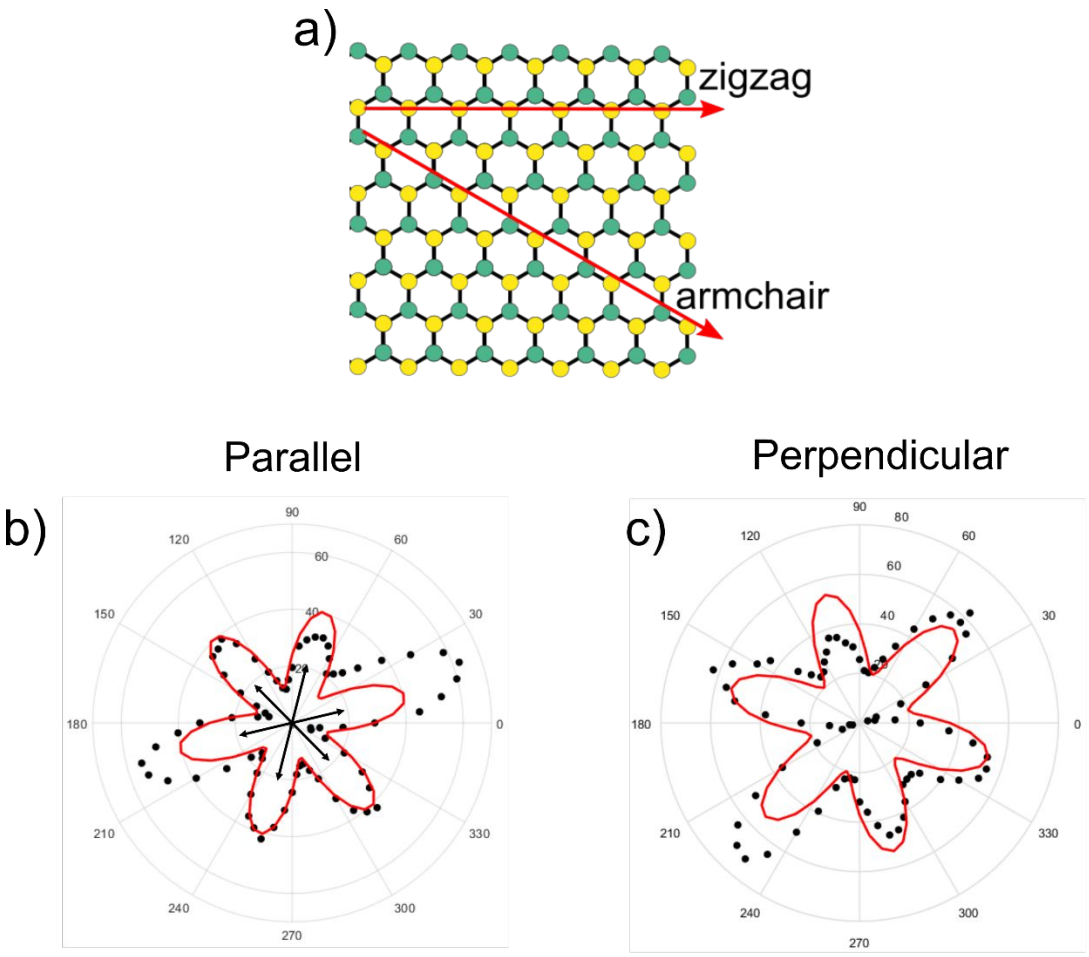

Figure S8 a) Illustration of the MoS_2 lattice depicting the high-symmetry armchair and zigzag directions. b) SHG results in the parallel polarization configuration for the monolayer region of MoS_2. The dots correspond to the data, and the red line corresponds to the $\cos^2(3\theta\text{-}3c)$ fit for c = 15°. The six arrows point from the origin along the three armchair directions determined from the SHG result. c) SHG results in the perpendicular polarization configuration. The red line corresponds to the $\sin^2(3\theta\text{-}3c)$ fit for c = 15°. For (b) and (c), zero degrees corresponds to the horizontal axis of AFM and KPFM measurements.

To account for a rotated lattice orientation in piezoelectricity calculations, we apply a rotation transformation to the coordinate system of the strain tensor such that the x and y components of the new coordinate system lie along an armchair and zigzag direction, respectively:

$$\varepsilon^{\theta} = R(\theta)\varepsilon^{0}R^{T}(\theta) \ , \tag{18}$$

where R and R^T are the transformation matrix for rotation by θ and its transpose. The polarization field is then calculated in the rotated coordinates before being rotated back to the original coordinate system via $P^0 = R^T(-\theta)P^{\theta}$, where P^0 and P^{θ} are the dielectric polarization field in the AFM coordinate system and the coordinate system rotated by θ, respectively. The piezoelectric bound charge is then calculated from P^0 according to $\sigma_{pz} = -\nabla \cdot \overrightarrow{P^0}$; however, either of P^0 or P^{θ} can be used, as the divergence is invariant under rotation.

In order to calculate the electrostatic potential generated by the piezoelectric bound charge distribution, we use the method of moments and the single point approximation.[19] Calculating the potential generated by the piezoelectric charge distribution yields the result in Figure S7a. While there is some resemblance between the electrostatic potential due to piezoelectricity and the KPFM measurement in proximity to the nanomesa, the potential extends farther from the area of large strain than in the KPFM measurements of the main text. Contributions of the piezoelectric charge to the electrostatic potential decay with distance according to 1/r in the unscreened solution; however, neglected in these calculations is screening caused by free carriers in the MoS_2 monolayer, which can screen out the potential generated by piezoelectric bound charges. Screening in monolayer MoS_2 does not follow the behavior of 3D Thomas Fermi screening with an effective screening length; rather, because the monolayer thickness is relatively comparable to the effective Bohr radius, screening must be considered for a 2D system. In the solution to the 2D screening problem, the potential decays with a $1/r^3$ dependence which can be approximated by:[20]

$$\varphi(r) = \frac{ea^2}{4\epsilon r^3}\left(\frac{m^* k_B T}{\pi n \hbar^2}\right)^2, \tag{19}$$

where a is the effective Bohr radius, ϵ is the permittivity of MoS_2, and n is the free carrier concentration.

The calculated electrostatic potential in the main text assumes screening with carrier concentration n=8x10^{10}cm^{-2}, which was chosen to approximately reproduce the peak potential variation of the unscreened solution. The screened solution alters the spatial distribution of the potential, mainly by confining the potential distribution to the bound charge distribution due to the 1/r^3 dependence. The screened potential more closely resembles the spatial distribution of V_t measured by KPFM at Vg=-1V.

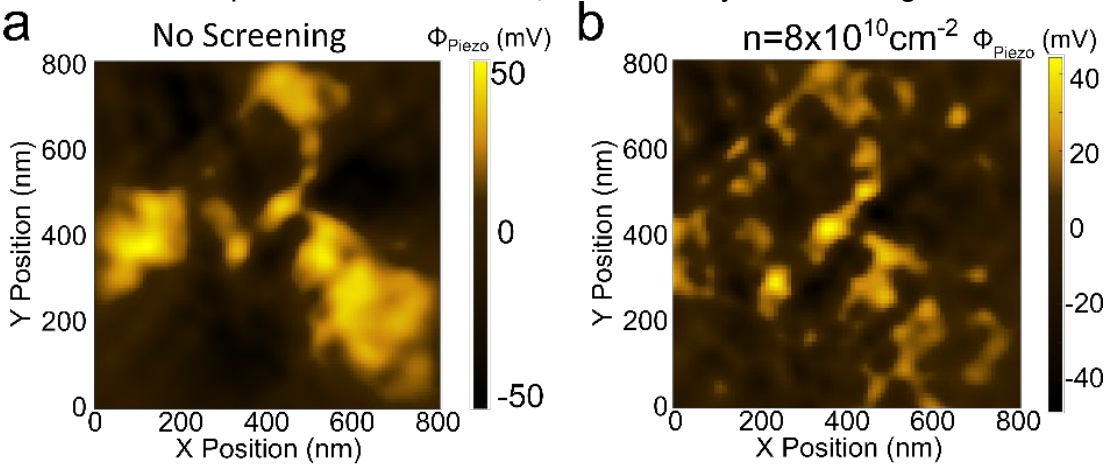

Figure S9. (a) Electrostatic potential due to the piezoelectric bound charge calculated assuming no screening. (b) Electrostatic potential due to the piezoelectric bound charge calculated assuming screening and carrier concentration n=8x10^{10}cm^{-2}.

S11 Alignment of KPFM Data:

We can better compare the position of the calculated piezoelectric potential and the KPFM measurement at V_g=-1V by alignment of the topography data acquired during KPFM measurements. An alignment algorithm was used to align KPFM images at different V_g to account for electrostatic and thermal drift between images. The corresponding height images from the first pass, which are relatively constant with respect to V_g excluding lateral drift, are used to compute the relative offset between two height images by finding the shift in x and y which minimizes the sum of the pixel-by-pixel difference between the two images. This offset is then applied to the corresponding AFM and KPFM images to enable better point to point comparisons across V_g. We align the

screened piezoelectric potential and V_t at V_g=-1V laterally using the offset computed between V_g=5V and V_g=-1V, as shown in Figure 5e of the main text.

S12 Other sites at 0V:

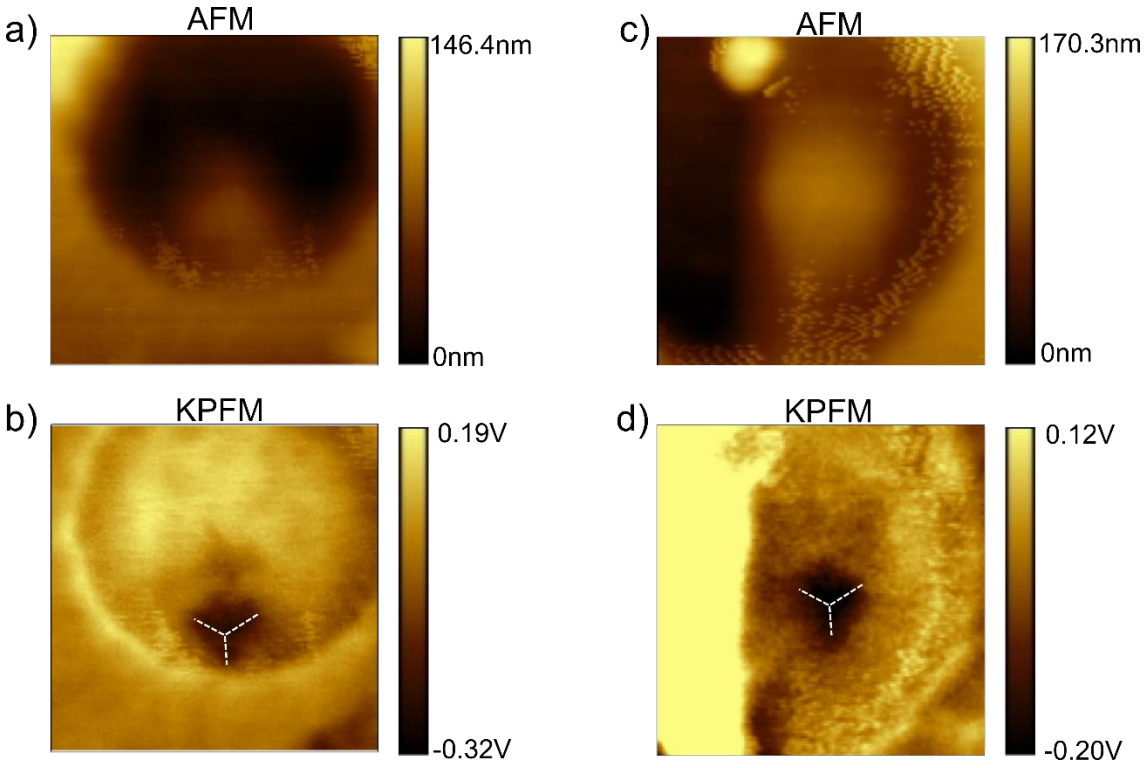

Figure S10. Characterization of strained monolayer MoS2 at differing locations from the main text. (a) and (b) are the AFM topography and corresponding KPFM at one location. (c) and (d) are the AFM topography and KPFM at a second location. A similar threefold symmetry near the top of the nanomesa, similar to that noted in the main text, can be seen in the KPFM images of both locations. The vertical line in KPFM contrast in d) is due to the boundary of the MoS2, which ends to the left of the nanomesa.

References:

(1) Hulteen, J. C.; Van Duyne, R. P. Nanosphere Lithography: A Materials General Fabrication Process for Periodic Particle Array Surfaces. *J. Vac. Sci. Technol. A Vacuum, Surfaces, Film.* **1995**, *13* (3), 1553–1558. https://doi.org/10.1116/1.579726.

(2) Haynes, C. L.; Van Duyne, R. P. Nanosphere Lithography: A Versatile Nanofabrication Tool for Studies of Size-Dependent Nanoparticle Optics. *J. Phys. Chem. B* **2001**, *105*, 5599–5611. https://doi.org/10.1177/074193258901000304.

(3) Li, P. C.; Yu, E. T. Flexible, Low-Loss, Large-Area, Wide-Angle, Wavelength-Selective Plasmonic Multilayer Metasurface. *J. Appl. Phys.* **2013**, *114* (13).

https://doi.org/10.1063/1.4824371.

(4) Li, X. H.; Li, P. C.; Hu, D. Z.; Schaadt, D. M.; Yu, E. T. Light Trapping in Thin-Film Solar Cells via Scattering by Nanostructured Antireflection Coatings. *J. Appl. Phys.* **2013**, *114* (4). https://doi.org/10.1063/1.4816782.

(5) Castellanos-Gomez, A.; Buscema, M.; Molenaar, R.; Singh, V.; Janssen, L.; Van Der Zant, H. S. J.; Steele, G. A. Deterministic Transfer of Two-Dimensional Materials by All-Dry Viscoelastic Stamping. *2D Mater.* **2014**, *1* (1). https://doi.org/10.1088/2053-1583/1/1/011002.

(6) Lee, C.; Yan, H.; Brus, L. E.; Heinz, T. F.; Hone, J.; Ryu, S. Anomalous Lattice Vibrations of Single- and Few-Layer MoS2. *ACS Nano* **2010**, *4* (5), 2695–2700. https://doi.org/10.1021/nn1003937.

(7) Li, H.; Zhang, Q.; Yap, C. C. R.; Tay, B. K.; Edwin, T. H. T.; Olivier, A.; Baillargeat, D. From Bulk to Monolayer MoS 2: Evolution of Raman Scattering. *Adv. Funct. Mater.* **2012**, *22* (7), 1385–1390. https://doi.org/10.1002/adfm.201102111.

(8) Mak, K. F.; Lee, C.; Hone, J.; Shan, J.; Heinz, T. F. Atomically Thin MoS2: A New Direct-Gap Semiconductor. *Phys. Rev. Lett.* **2010**, *105* (13), 2–5. https://doi.org/10.1103/PhysRevLett.105.136805.

(9) Büttiker, M.; Thomas, H.; Prêtre, A. Mesoscopic Capacitors. *Phys. Lett. A* **1993**, *180* (4–5), 364–369. https://doi.org/10.1016/0375-9601(93)91193-9.

(10) Wiktor, J.; Pasquarello, A. Absolute Deformation Potentials of Two-Dimensional Materials. *Phys. Rev. B* **2016**, *94* (24), 1–8. https://doi.org/10.1103/PhysRevB.94.245411.

(11) Pearce, A. J.; Mariani, E.; Burkard, G. Tight-Binding Approach to Strain and Curvature in Monolayer Transition-Metal Dichalcogenides. *Phys. Rev. B* **2016**, *94* (15). https://doi.org/10.1103/PhysRevB.94.155416.

(12) Johari, P.; Shenoy, V. B. Tuning the Electronic Properties of Semiconducting Transition Metal Dichalcogenides by Applying Mechanical Strains. *ACS Nano* **2012**, *6* (6), 5449–5456. https://doi.org/10.1021/nn301320r.

(13) Darlington, T. P.; Krayev, A.; Venkatesh, V.; Saxena, R.; Kysar, J. W.; Borys, N. J.; Jariwala, D.; Schuck, P. J. Facile and Quantitative Estimation of Strain in Nanobubbles with Arbitrary Symmetry in 2D Semiconductors Verified Using Hyperspectral Nano-Optical Imaging. *J. Chem. Phys.* **2020**, *153* (2). https://doi.org/10.1063/5.0012817.

(14) Landau, L. D.; 1986.

(15) Mai-Duy, N.; Tanner, R. I. A Spectral Collocation Method Based on Integrated Chebyshev Polynomials for Two-Dimensional Biharmonic Boundary-Value Problems. *J. Comput. Appl. Math.* **2007**, *201* (1), 30–47. https://doi.org/10.1016/j.cam.2006.01.030.

(16) Duerloo, K. A. N.; Ong, M. T.; Reed, E. J. Intrinsic Piezoelectricity in Two-Dimensional Materials. *J. Phys. Chem. Lett.* **2012**, *3* (19), 2871–2876. https://doi.org/10.1021/jz3012436.

(17) Malard, L. M.; Alencar, T. V.; Barboza, A. P. M.; Mak, K. F.; De Paula, A. M. Observation of Intense Second Harmonic Generation from MoS2 Atomic Crystals. *Phys. Rev. B - Condens. Matter Mater. Phys.* **2013**, *87* (20), 1–5. https://doi.org/10.1103/PhysRevB.87.201401.

(18) Liang, J.; Zhang, J.; Li, Z.; Hong, H.; Wang, J.; Zhang, Z.; Zhou, X.; Qiao, R.; Xu, J.; Gao, P.; Liu, Z.; Liu, Z.; Sun, Z.; Meng, S.; Liu, K.; Yu, D. Monitoring Local Strain Vector in Atomic-Layered MoSe2 by Second-Harmonic Generation. *Nano Lett.* **2017**, *17* (12), 7539–7543. https://doi.org/10.1021/acs.nanolett.7b03476.

(19) Dworsky, L. N. *Introduction to Numerical Electrostatics Using MATLAB®*; 2014. https://doi.org/10.1002/9781118758571.

(20) Rytova, N. S. Screened Potential of a Point Charge in a Thin Film. **1967**, No. January 1967.